ORNL/TM-2023/2843

Design and Testing of the Vortex Ring Facility

Duy Thien Nguyen
Nolan Goth
Pablo Moresco
Vincent Jodoin
Vivek Rao

April 2023

OAK RIDGE National Laboratory

ORNL IS MANAGED BY UT-BATTELLE LLC FOR THE US DEPARTMENT OF ENERGY

ORNL/TM-2023/2843

Nuclear Energy and Fuel Cycle Division

DESIGN AND TESTING OF THE VORTEX RING FACILITY

Duy Thien Nguyen
Nolan Goth
Pablo Moresco
Vincent Jodoin
Vivek Rao

April 2023

Prepared by
OAK RIDGE NATIONAL LABORATORY
Oak Ridge, TN 37831
managed by
UT-Battelle LLC
for the
US DEPARTMENT OF ENERGY
under contract DE-AC05-00OR22725

CONTENTS

LIST OF FIGURES

LIST OF TABLES

ABBREVIATIONS

ASME	American Society of Mechnical Engineers
BOS	background-oriented Schlieren
CFD	computational fluid dynamics
CFL	Courant–Friedrichs–Lewy
DEHS	diethylhexyl sebacate
DIC	digital image correlation
fps	frame per second
LES	large eddy simulation
NQA	Nuclear Quality Assurance
ORNL	Oak Ridge National Laboratory
PIV	particle image velocimetry
PMMA	poly(methylmethacrylate)
VOF	volume of fluid

ABSTRACT

This document summarizes the efforts of building an experimental test facility to study the evolution of the cloud following a nuclear detonation above ground level and support the development of numerical models to describe it. The experimental facility allows nonintrusive flow visualization and measurements of buoyant vortex ring formation and evolution using background-oriented Schlieren and particle image velocimetry techniques.

In addition, 3D unsteady computational fluid dynamics simulations using unsteady Reynolds-averaged Navier–Stokes and volume-of-fluid numerical methods were performed to support the experimental design as well as to provide insight about the formation and evolution of the vortex ring.

1. INTRODUCTION

Shortly after an aboveground nuclear device detonation, a convective cloud develops, and its motion can be observed by the entrainment of dust, debris, and in some cases, water condensation. An aboveground nuclear detonation can be approximated by an almost instantaneous release of energy in a confined volume of air, yielding in a high temperature and low density perturbation of the atmosphere (Moresco et al. (2014); Moresco (2022)). The nuclear cloud accelerates because of the buoyant force created by the significant difference in density between the core of the cloud and the surrounding atmosphere. This motion entrains cooler and denser air. Eventually, the cloud speed decreases monotonically, and its height stabilizes when it becomes neutrally buoyant.

Morton et al. (1956) and Turner (1957) laid the theoretical baseline for nuclear cloud rise through the evolution of buoyant spheres and vortex rings. Turner (1957) suggested using the characteristics of these flows to describe thermals and buoyant clouds. Additional complexities have been investigated since then, such as the consideration to account for stratification of the atmospheric density by Caulfield and Woods (1998). Many empirical studies also suggest a similarity between instantaneous releases of buoyant fluid developing into recirculating flows and vortex rings. In descriptions of the fallout distribution, Foster (1982) argued that it is vital to accurately predict the evolution and motion of the nuclear cloud provided the weapon yield, emplacement, and atmospheric conditions at the time of detonation.

In recent numerical efforts, Won and Lee (2020) have performed large eddy simulations (LES) and Arthur et al. (2021) have studied the viability of using the Weather Research and Forecasting model to predict nuclear cloud rise. Also, Moresco (2022) has developed a formulation of the nuclear cloud that is intermediate in computational cost and based on a vortex ring formulation and a full solution of the equations of motion. In this approach, a series of approximations are made to reduce the model's complexity while maintaining the ability to resolve most features of interest. A set of constraints (Shariff and Leonard (1992)) are then introduced to reduce the number of degrees of freedom of the system. This level of computational expense can be handled with a standard personal computer and provides results within minutes to hours, that is within the time frame for emergency response and forensic analysis activities.

Moresco (2022) also defined the vortex ring flow description based on the vorticity field. This refined the computational expense of the method to small regions of high relative vorticity. Despite axisymmetric and swirl-free flow assumptions, the formulation can estimate the 3D velocity distribution by combining the velocity field induced by the ring with atmospheric winds. Such feasibility could approximate the transport of scalar quantities, such as the water vapor mixing ratio, temperature, and the condensed phase of

Lagrangian particles representing fallout. Moresco (2022) concluded that during most of buoyant vortex ring evolution, the core is turbulent, and a better understanding of its stability is essential to improve the accuracy of the simulated cloud evolution. Validation with appropriate experimental studies of buoyant vortex rings is needed to improve this approach and increase confidence in its predictive capabilities.

The objective of this and future work is to develop an experimental test facility to study the evolution of buoyant vortex rings with lower density cores, which are the dominant structures during the evolution of nuclear clouds. This setup is intended to support the development and validation of cloud models with different degrees of complexity and based on a variety of approximations using data about the ring properties as a function of time, including vorticity distributions and stability characteristics. Although buoyant vortex rings have been studied experimentally in the past, those setups were mostly restricted to small density differences between the ring core and its environment and tended to focus on negative buoyancy configurations (higher density cores). The test facility design is described in Section 2, experimental measurements are presented in Section 3, and numerical results using computational fluid dynamics (CFD) can be found in Section 4.

2. VORTEX RING EXPERIMENTAL TEST FACILITY

The facility was designed to facilitate studies of buoyant vortex rings generated by the sudden release of a light gas in an environment containing heavy gas. Figure 1 presents an overview of the facility, which consists of a transparent test section enclosing the heavy gas. Figure 2 illustrates one of several studied light gas release mechanisms. A similar cup release method was employed using liquids by Scorer (1957) and Thompson et al. (2000). The release mechanism shown is modular to allow different sized cups to be attached to a fast-acting stepper motor controlled to rotate 180°at a speed of 3,000 rpm. Cups with diameters of 25, 50, 75, and 100 mm were tested in this effort. The lessons learned from various release methods, including the cup, balloon burst, and bubble burst, are discussed in Section 2.1.

The test section was supported by T-slot extruded aluminum rails and had a total height of 1,220 mm (4 ft) and a cross section of 610×610 mm^2 (2×2 ft^2). It was made of transparent poly(methyl methacrylate) (PMMA), which is commonly known as acrylic. The transparent walls allowed for nonintrusive flow visualization measurements to be performed using light sources (high-power LEDs, lasers, or both) and cameras. The front panel of the test facility is removable to allow access to the interior when preparing the experimental measurements.

Several gas pairs were identified to achieve various light-to-heavy gas density ratios while also being inert, relatively low cost, and compatible with optical flow measurement techniques. Table 1 lists such pairs of light (ρ_1) and heavy (ρ_2) inert gases with density ratios from 7.38 to 67.13 that were identified for the vortex ring test facility. In the current study, experimental measurements of buoyant vortex ring evolutions were performed using the helium/nitrogen gas pair at an atmospheric pressure associated with 850 ft above sea level and at a temperature of 21°C. This selection was made because it would capture the relevant phenomena and demonstrate the ability of the facility while using readily available and low cost gases.

The test section has several 3 and 6 mm bulkhead fittings to allow for several operations. One connection on the top panel supplies the heavy gas via a compressed gas cylinder for the sweeping and inerting process. This process involved displacing the volume of air within the test section with the desired heavy gas. The air was pneumatically exhausted through a line with an O_2 sensor. The test section was considered sufficiently inerted when the O_2 sensor reported that the exhausted gas contained less than 1% O_2.

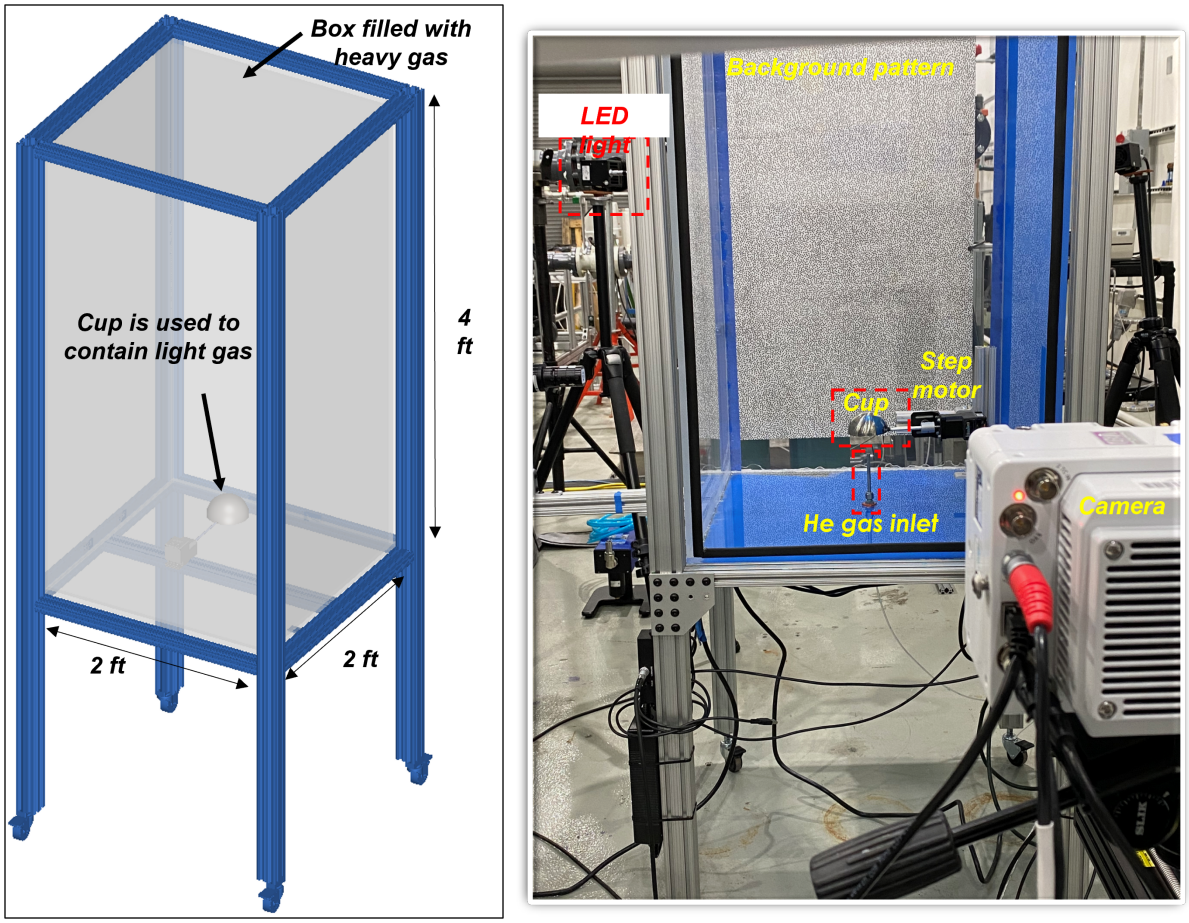

Figure 1. Experimental facility of buoyant vortex ring (left) CAD design, and (right) a photo of facility.

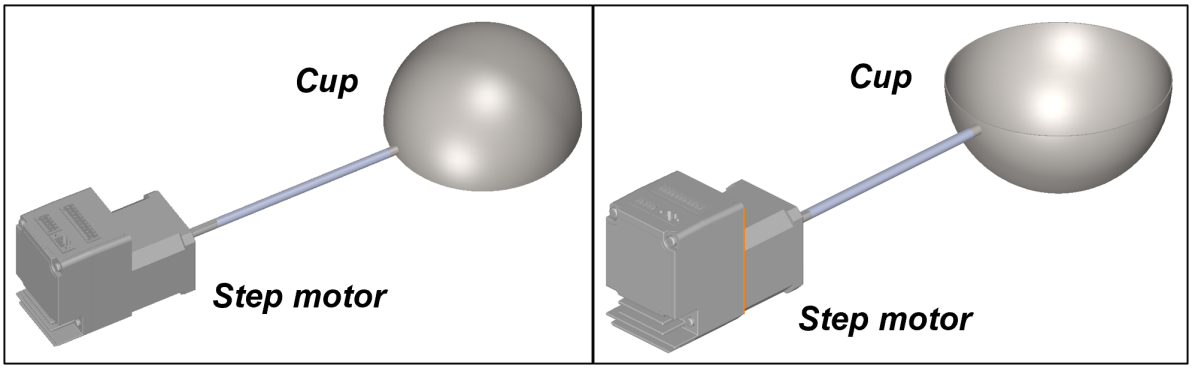

Figure 2. Design of the cup release mechanism. The cup is connected to a stepper motor to (left) contain the light gas and (right) then release it by rotating 180°, allowing buoyancy-driven flow to develop.

Table 1. Pairs of light (ρ_1) and heavy (ρ_2) inert gases considered for experimental measurements in the vortex ring test facility.

Option	Light gas	Heavy gas	Density ratio (ρ_2/ρ_1)
1	helium (ρ_{He} = 0.167 kg/m^3)	nitrogen (ρ_{N_2} = 1.232 kg/m^3)	7.4
2	nitrogen (ρ_{N_2} = 1.232 kg/m^3)	perfluorobutane (ρ_{PFB} = 11.21 kg/m^3)	9.1
3	helium (ρ_{He} = 0.167 kg/m^3)	sulfur hexafluoride (ρ_{SF_6} = 6.17 kg/m^3)	36.9
4	helium (ρ_{He} = 0.167 kg/m^3)	perfluorobutane (ρ_{PFB} = 11.21 kg/m^3)	67.1

Another top panel connection is connected to a bubbler system, which passively manages the internal pressure of the test section and provides the safety-related pressure relief function. A bottom panel connection leads to a three-way valve. This valve can be positioned to either act as a gas outlet or inlet. The outlet valve position leads to an oxygen sensor to monitor the efficacy of the sweeping and inerting processes. The inlet valve position aligns the test section to the light gas compressed cylinder.

Images were captured during the period surrounding the cup rotation or bubble burst using a high-speed camera such as the Phantom VEO 440, which is capable of 1,100 Hz at a resolution of 2,560 × 1,600 pixels. A digital timing synchronizer, such as LaVision's PTU-X is used to temporally align the trigger timing sequences of the camera and light source. Available light sources for this facility include high-intensity DC-powered LEDs with 15,000 lm output and a dual pulsed laser at 532 nm with 200 mJ output at 15 Hz.

2.1 LIGHT GAS RELEASE METHODS

Three light gas release methods were investigated. The first was the downward-facing cup. This was chosen because of its apparent success in the related buoyancy-driven liquid flow studies of Scorer (1957). The method involved orienting the cup with its concave surface pointed downward (c.f., Figure 2(left)). Next, heavy gas flowed into the the test section to inert the facility. The displaced air was directed to an oxygen sensor for a concentration measurement and then into the lab space. The light gas was then slowly injected into the cup using Parker mass flow controllers to provide the desired mass and volume to be released. For this release method, a programmed motion of the stepper motor rotated the cup 180°to initiate the release of light gas into the ambient heavy gas.

However, gases have a zero or near-zero attractive force between similar molecules. This, along with a very buoyant light gas, presented challenges for filling the cup and visualizing the release. Even with a small injection rate, such as filling the cup volume over a 3 minute time period, only a small amount of helium was contained within the cup. This could be a combination of gas momentum created by the jet injection, diffusion of gases, and the buoyancy effect of the light gas. It could also be attributed to the momentum imparted onto the light gas by the shear-induced motion from the cup surface rotating. Regardless of the mechanism of disturbance, the cup release method resulted in light gas flow fields with concentrations less than the BOS visualization threshold.

The second and third release methods were light gas–containing latex rubber balloons and soap bubbles. The balloon method could be successfully filled with the light gas and the amount was significantly above the visualization threshold for BOS. However, the balloons had a relatively thick skin and required a large enough internal pressure to rupture the skin with a needle. This internal pressure led to an undesirable initial condition with isotropic expansion of the light gas. The stored energy of the elastomer balloon likely

imparted momentum to the internal light gas and external heavy gas upon rupture. This was observed to be very different from the desired initial condition of release that could develop into the expected buoyancy-driven vortex ring phenomena.

To reduce the internal pressure and stored energy, light gas–filled soap bubbles were tested as the third method. This was an effective method because of the lower surface tension and reduction of the internal pressure which avoided isotropic expansion and was still above the BOS visualization threshold. For this release method, the bubble was filled until an approximate desired diameter was reached using a ruler with 1 mm markings placed within the camera's field of view. The injection of light gas was then stopped, and the bubble was allowed to burst on its own. Several bubbles were attempted, and the bubble's size depended on the size of nozzle used. In this study, the nozzle had an opening of 13 mm, and the bubble's diameter was approximately 25 mm.

3. EXPERIMENTAL MEASUREMENTS OF VORTEX RING

Two measurement techniques were employed in this effort, namely BOS and particle image velocimetry (PIV). These techniques are discussed in Sections 3.1 and 3.2, while results can be found in Section 3.3.

3.1 BACKGROUND-ORIENTED SCHLIEREN TECHNIQUE

To qualitatively characterize the evolution of the buoyancy-driven vortex ring in the test facility, the BOS technique was applied. The experimental setup of the BOS measurement is illustrated in Figure 3 and includes a high-speed camera, background panels of randomly generated dots positioned behind the test facility, and high-power LED lights to illuminate the random dot pattern.

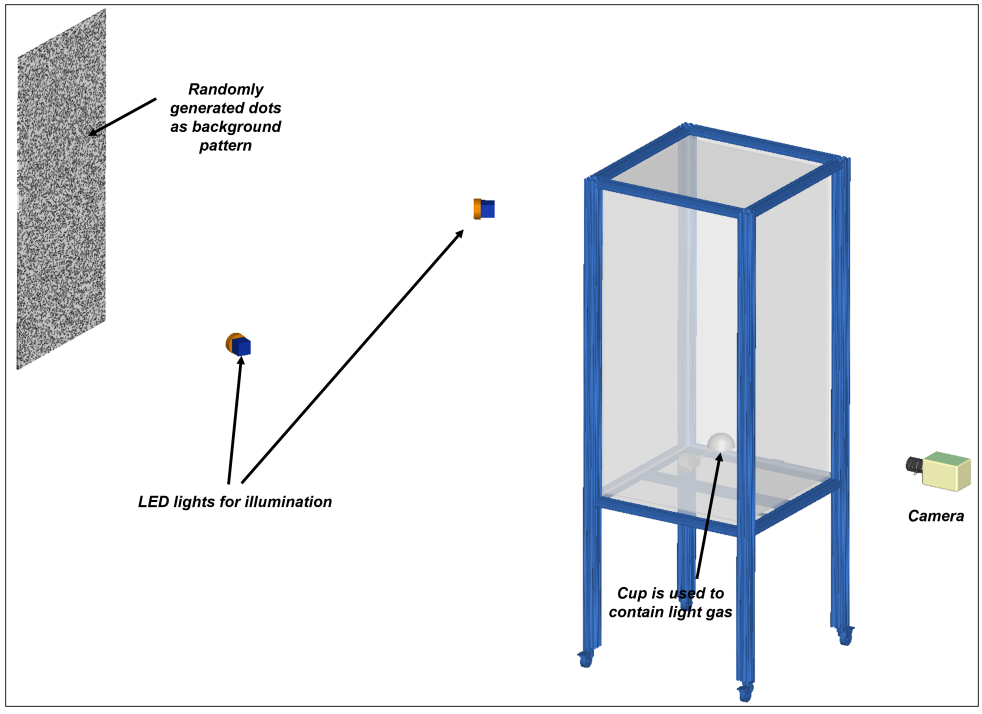

Figure 3. Background-oriented Schlieren (BOS) setup for the vortex ring test facility.

BOS is an optical density visualization technique that applies a digital image correlation approach on a background pattern to qualitatively and quantitatively characterize thermal-fluid flow behaviors (Raffel (2015)). The BOS technique is based on the relation between the refractive index of a fluid (liquid/gas) and its density, given by the Lorentz–Lorenz equation, which can be simplified to the Gladstone–Dale equation for gaseous media (Raffel (2015)). This means that the physical quantity being directly observed is the refractive index and the impact of a dynamic index integrated along the line of sight between a camera and a static background pattern. This quantity is temperature-, density-, and wavelength-dependent. Therefore, differences in temperature and density can be indirectly observed with this optical technique. An advantage of BOS is the simplicity of the setup and the robustness of correlation-based analysis. These inherent characteristics make it useful and widely applied to various types of compressible and incompressible flows with good spatial and temporal resolutions, which depend primarily on the imaging hardware.

As illustrated in Figure 4, an experimental setup for BOS measurements consists of a camera with a standard camera lens, a background pattern, and the object or volume of interest with a different density between the camera and the background pattern. The camera viewing direction is perpendicular and focused on the background pattern. The distance between the camera and the background pattern can be used to adjust the field of view and magnification of the image on the camera sensor.

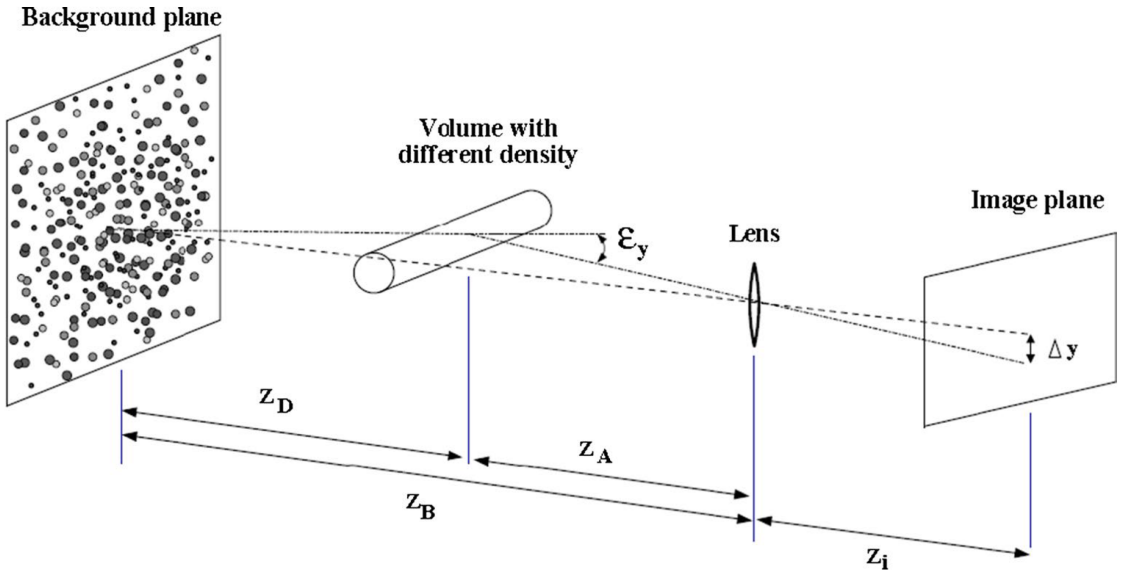

Figure 4. Imaging configuration for the BOS technique (Raffel (2015)).

The recording procedure begins with capturing a reference image of the background pattern with no density difference in the line-of-sight between the camera and background pattern. Next, images are captured for the flow under investigation. The images with a density difference in the region of interest will contain local displacement of the dot pattern relative to the reference image. The resulting reference and experimental images can then be processed using image correlation methods. The cross-correlation algorithm developed and optimized for the PIV technique can be applied to determine the displacement of patterns at multiple spatial locations throughout the entire image (Raffel et al. (1998); Raffel (2015)).

In Figure 4, the deflection of light due to the density difference spatially located at the volume of interest can be related to the spatial gradient of the refractive index integrated along the line of sight. Further details

about the theory of ray tracing can be found in studies of Sharma et al. (1982) and Dorić (1990).

Assuming axially parallel recording and a small deflection angle, ε_y, such that $\varepsilon_y \approx \tan \varepsilon_y$ is appropriate, then a displacement, Δy, between reference image and experimental image set can be computed. This is derived for the BOS technique (Raffel et al. (1998)) as

$$\Delta y = Z_D M \varepsilon_y, \tag{1}$$

where $M = Z_i/Z_B$ is the magnification factor of the background, Z_D is the distance between the dot pattern and the region with a density gradient, and ε_y is the deflection angle that can be expressed as

$$\varepsilon_y = \frac{1}{n_0} \int \frac{\partial n}{\partial y} dz. \tag{2}$$

The image displacement Δy can be then written as

$$\Delta y = f \left(\frac{Z_D}{Z_D + Z_A - f} \right) \varepsilon_y, \tag{3}$$

where Z_A is the distance from the lens to the object of study and f is the focal length of the lens. Because the camera must be focused on the background pattern, f can be expressed by

$$\frac{1}{f} = \frac{1}{Z_i} + \frac{1}{Z_B}. \tag{4}$$

From Equation 3, a large image displacement can be achieved for a large Z_D and a small Z_A. Certain constraints in the decrease in Z_A need to be satisfied for imaging the flow field with sufficient sharpness. The optical imaging system should focus on the background patterns to obtain maximum contrast at high spatial frequencies for image interrogations, and in this case Equation 4 applies. The sharp imaging of the density gradients is obtained at Z_i' with

$$\frac{1}{f} = \frac{1}{Z_i'} + \frac{1}{Z_B}. \tag{5}$$

As the imaging system is focused on the background patterns, the sharpness of the investigated volume with a nonzero density gradient can be limited. The geometric blur, d_i, in Figure 5 can be expressed as

$$d_i = d_A \left[1 - \frac{1}{f} M' \left(Z_A - f \right) \right], \tag{6}$$

where d_A is the aperture diameter and $M' = Z_i'/Z_A$ is the density gradient imaging magnification. The following equation applies for the diffraction limited minimum image diameter, d_d, as

$$d_d = \frac{2.44 f}{d_A (M + 1) \lambda}, \tag{7}$$

where λ is the wavelength of the light ($\sim$ 550 nm). The overall image blur, $d_\sum$, can be approximated as

$$d_\sum = \sqrt{d_d^2 + d_i^2}. \tag{8}$$

In a typical BOS experimental setup, small aperture diameters are used to reduce the geometric blur, d_i. A small aperture limits the amount of illumination available to the camera sensor, increasing the demand for high-intensity background illumination. Because BOS processing also uses correlation techniques that average over the interrogation area, the overall image blur, $d_\sum$, does not yield a significant loss of information, provided that $d_\sum$ is smaller than the interrogation window size.

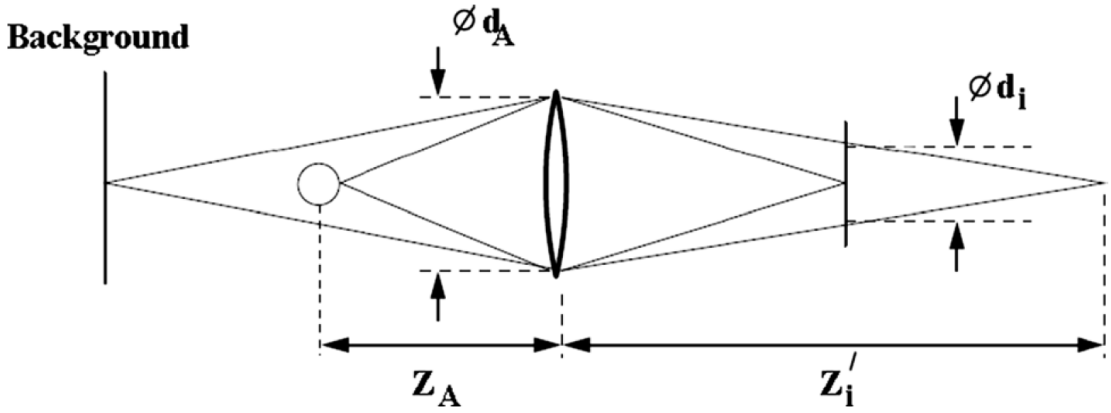

Figure 5. BOS focusing position and image blur (Raffel (2015)).

3.2 PARTICLE IMAGE VELOCIMETRY TECHNIQUE

PIV is a nonintrusive optical method of flow visualization that has been developed during the last 20 years. PIV can provide a quantitative measurement of the instantaneous velocity field across a planar area or volume of a flow field. For velocity measurements using this approach, the fluid is seeded with microscopically small, monodisperse particles with an appropriate size and density such that they follow the macroscopic motion of fluid elements without perturbing the flow or fluid properties. The tiny, neutrally buoyant particles—so-called "tracers"—can be tailored as needed. Examples include oil or water aerosols in air and solid particles in fluids, such as silver-coated hollow glass spheres.

The seeded flow is illuminated using a planar area or volume, normally formed by passing a laser beam (double pulsed laser or continuous laser) through an optical system of a collimator and cylindrical lenses. Particles in the flow are illuminated twice with a small time separation (i.e., Δt). A camera positioned perpendicular to the plane of the light sheet (oblique to the laser plane/volume if stereoscopic or tomographic PIV is applied) is shuttered to capture the light scattered from the illuminated particles (see Figure 6 (top)). At both instants of time, t and $t + \Delta t$, the particle positions are captured by the camera. The recorded particle displacement field is computed locally across the whole field of view of the images by applying PIV image cross-correlation algorithms (see Figure 6 (bottom)), scaled by the image magnification and then divided by the known pulse separation to obtain flow velocity at each point (Raffel et al. (1998)). Depending on the flow velocity and the factor of magnification of the camera lens, the time interval of the two pulses should be carefully chosen so that adequate displacements of the particle images are obtained. In many cases, what is adequate depends on the flow under investigation. In general, a displacement equal to 25% of the final pass interrogation window is nearly ideal, as long as the interrogation window size and Δt are selected to minimize nonlinear particle motion and displacement gradients at the local level (Raffel et al. (1998)). Using this selected Δt and the computed displacement of the particles, velocity vectors can then be calculated.

3.3 EXPERIMENTAL RESULTS

This section presents experimental results obtained from BOS and PIV measurements of buoyant vortex rings using the helium-filled bubble approach. A 3 mm tube and compression nut with a bore diameter of

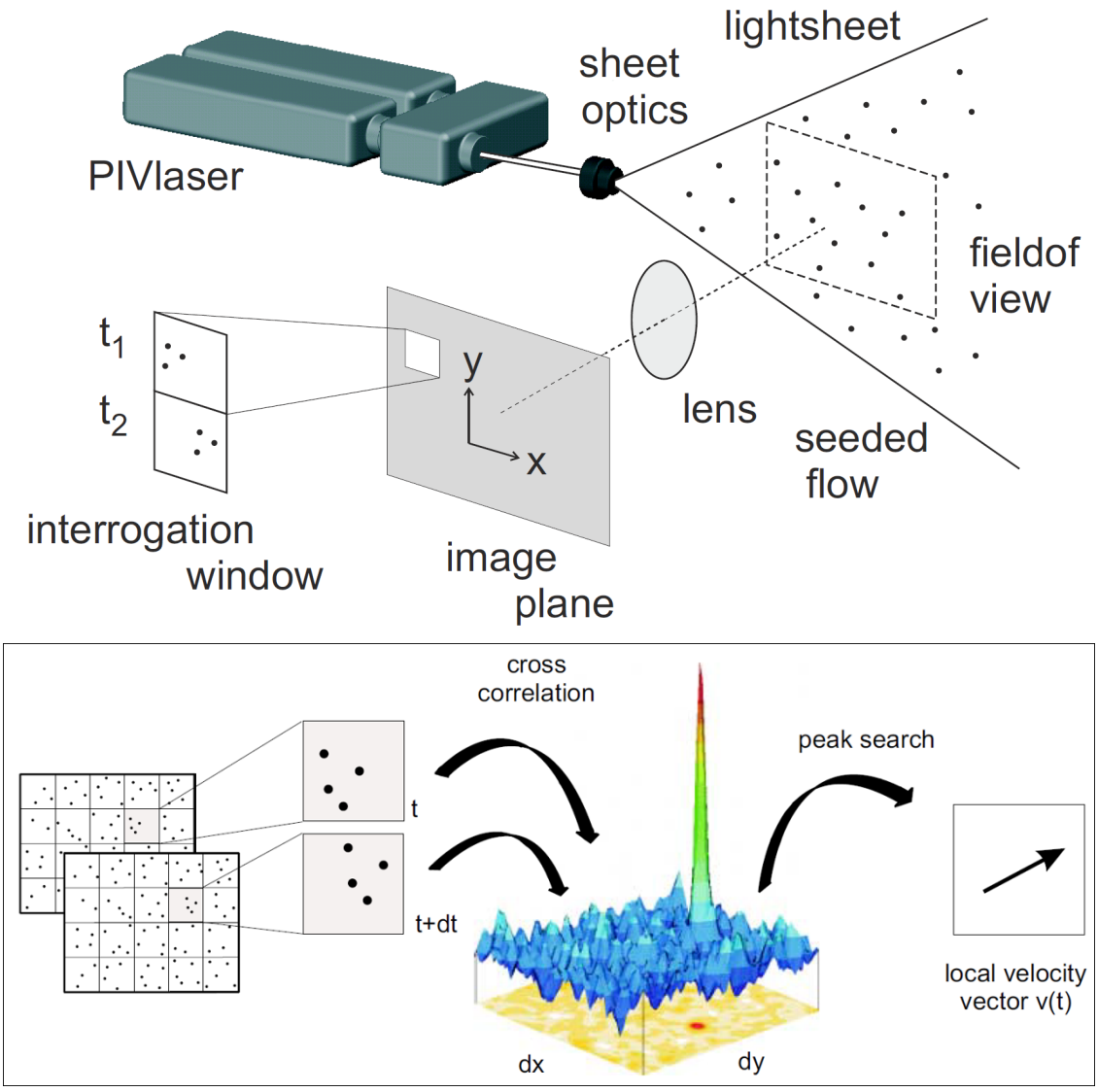

Figure 6. (Above) Setup of 2D two-component PIV measurements and (below) evaluation of PIV images using cross correlation (LaVision (2022)).

12.7 mm (see Figure 7) were used as the injection nozzle to create the helium bubbles. The bubbles were grown to a diameter of approximately 25.4 mm by applying a film of soap to the nut and slowly injecting helium through the nozzle. The gas injection process continued until the bubble reached the desired size. Next, the triggers for the light and imaging hardware were energized a few seconds before the helium-filled bubble burst. After the burst of the bubble's surface, the internal volume of helium gas would begin to buoyantly rise because of the density difference with the surrounding heavy gas. Consequently, the vortex ring would begin to form and eventually establish and evolve as it continued to rise. In this study, sequential images of the filling process, bubble burst event, and evolution of the buoyant vortex ring evolution were taken at 200 frames per second (fps) with a resolution of 2,560 × 1,600 pixels.

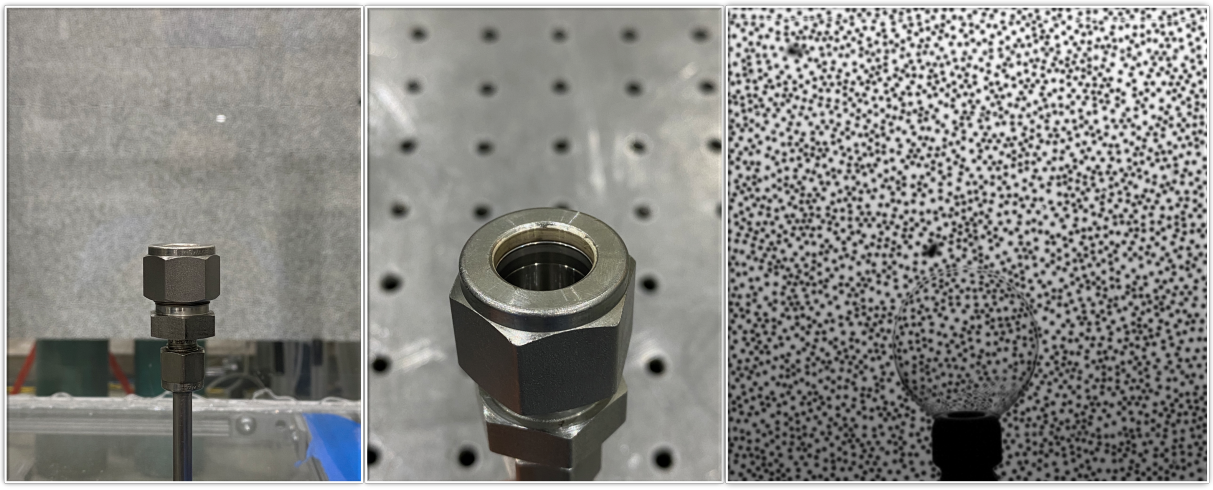

Figure 7. An alternative approach using helium-filled bubble for vortex ring experiment. (Left–middle) Nozzle used to create (right) helium-filled bubble for BOS measurement of vortex ring. The the bubble boundary and randomly generated dots of background patterns can be clearly seen.

Figure 8 illustrates a sequence of raw images captured using the high-speed camera at time instants of 0, 5, 10, and 35 ms into the burst. These images were processed using DaVis 10.2.1 software to obtain the displacement of the background dot patterns caused by the difference in refractive index between the two gases to visualize the motion of the light gas and vortex ring evolution. Figures 9–10 present results obtained from BOS postprocessing that yielded the pixel displacement fields at various times. The image series following the breakdown of the bubble shows the helium gas volume immediately migrating in the vertical direction because of the buoyant force. The nearly spherical volume transitioned to a mushroom shape in approximately two bubble diameters from the nozzle. Additionally, a counter-rotating vortex core was observed inside the cloud. The size and shape of the vortex core was found to dynamically change as the ring evolves. As the vortex ring moved along the vertical direction, smaller features detached, leaving a trail of elongated structures.

The ability to quantitatively obtain the velocity of vortex ring structures is crucial to understanding the cloud evolution process for various initial conditions. Several velocimetry techniques, which use BOS displacement fields and derived results as an input, have been proposed (Bühlmann et al. (2014); Xue et al. (2014); Settles and Liberzon (2022)). For instance, Bühlmann et al. (2014) suggested to apply PIV analysis to the BOS displacement field using the density gradient data as the tracer particles, and Settles and Liberzon (2022) successfully applied the digital image correlation algorithm (similar to PIV approach) to

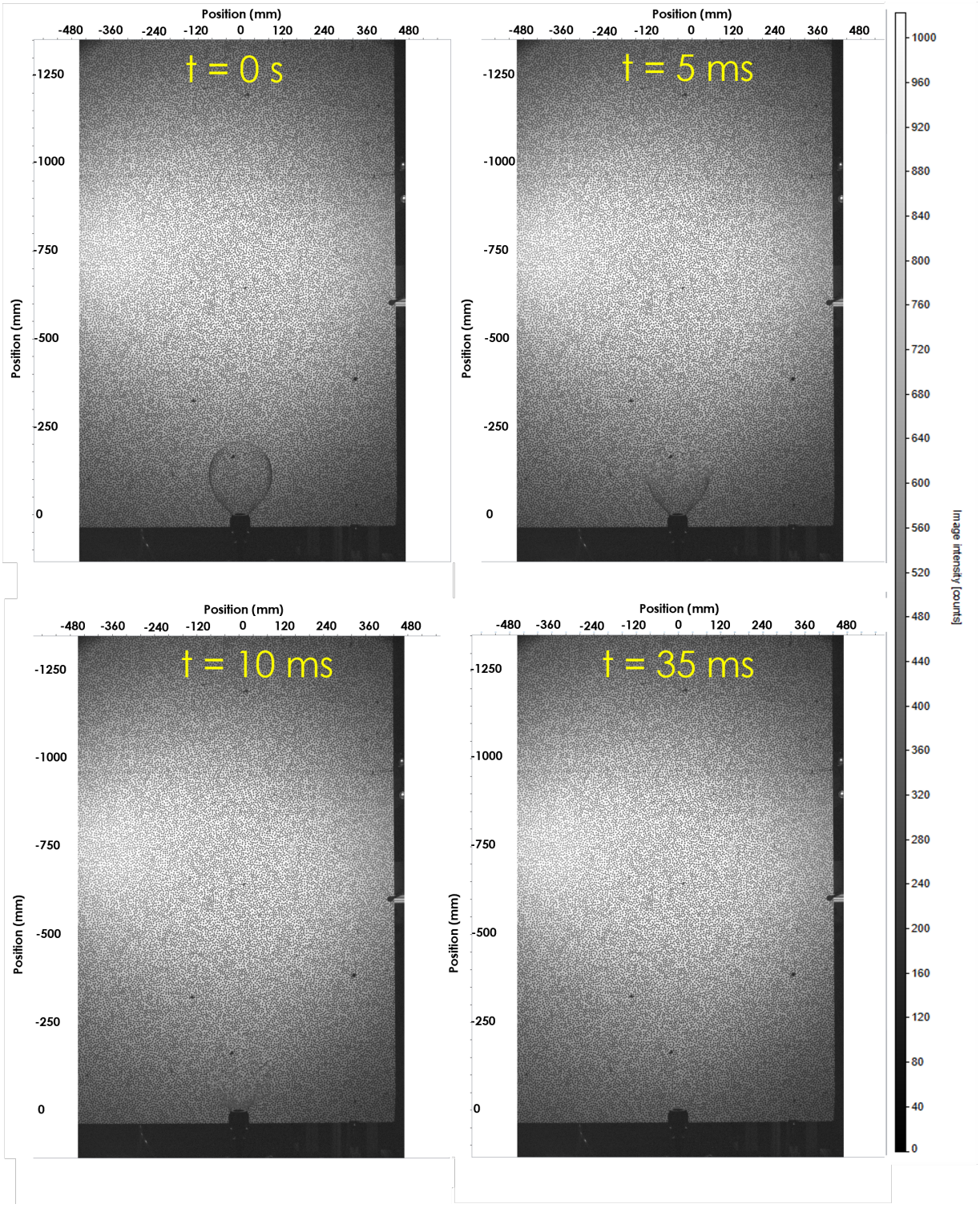

Figure 8. Experimental raw images of helium-filled bubble burst and buoyant vortex ring formation.

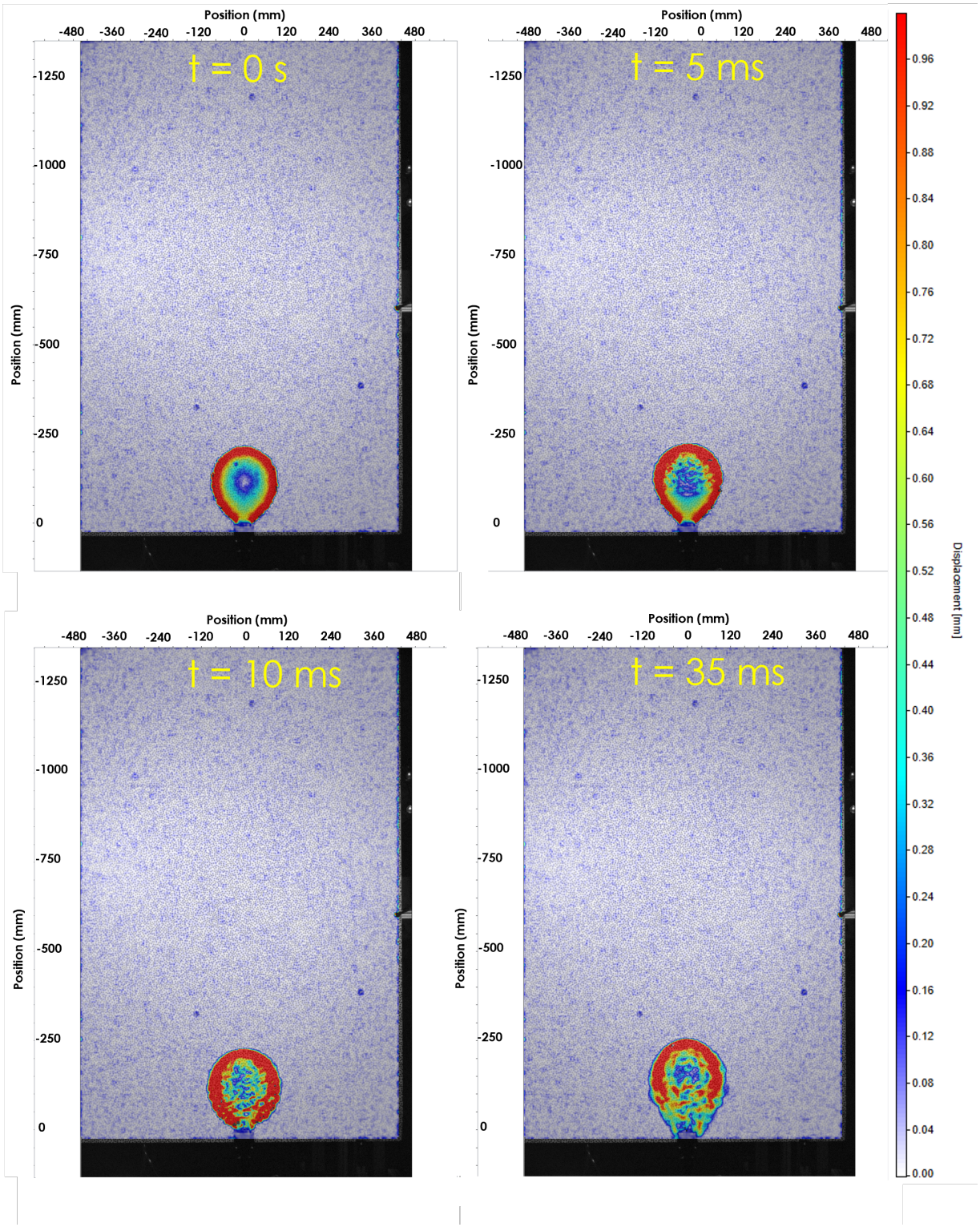

Figure 9. Experimental results obtained from postprocessing images with BOS. Color contours display displacements of background patterns caused by the evolution of a buoyant vortex ring (continued next page).

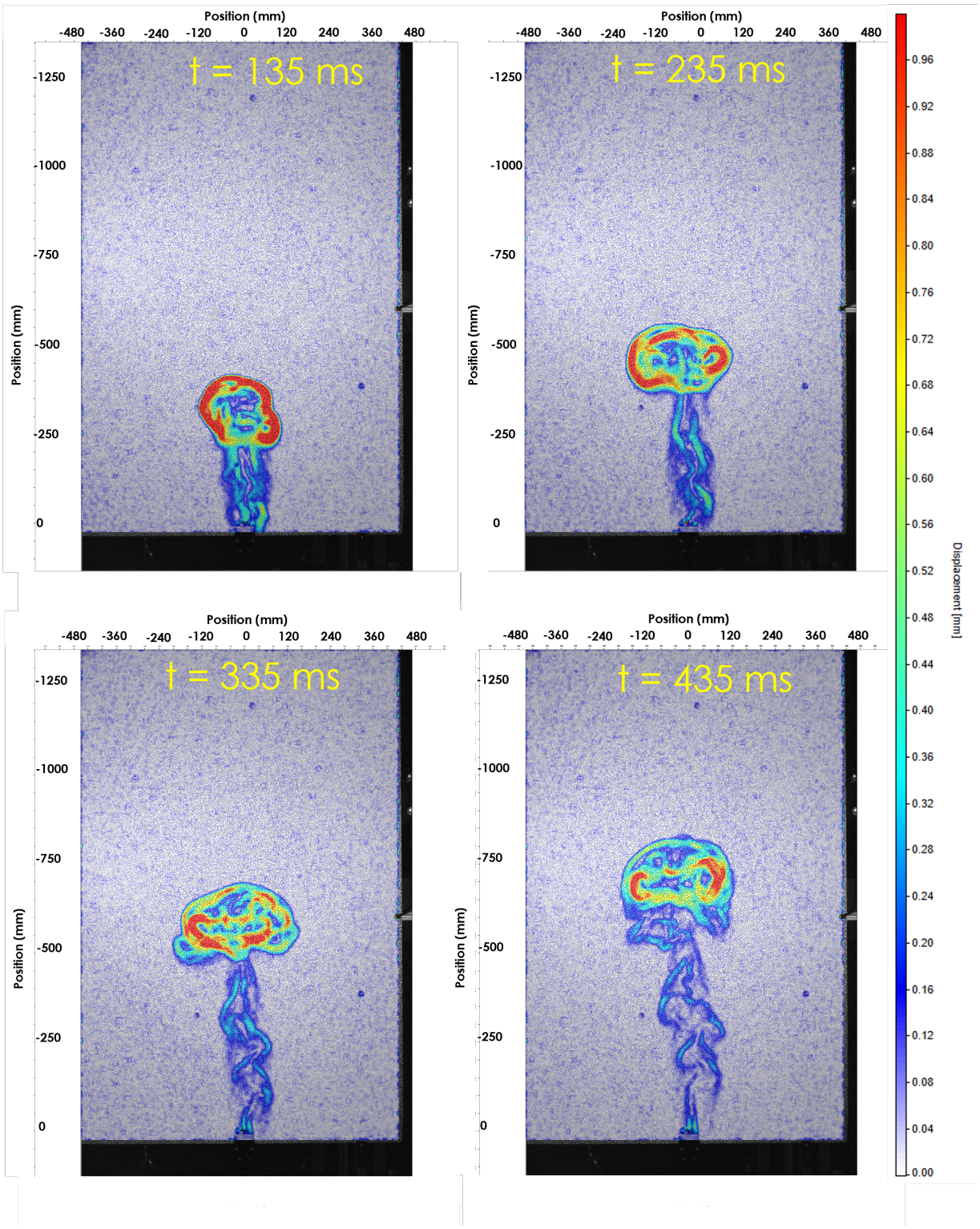

Figure 10. Experimental results obtained from postprocessing BOS images. Color contours display displacements of background patterns caused by the evolution of a buoyant vortex ring (from previous page).

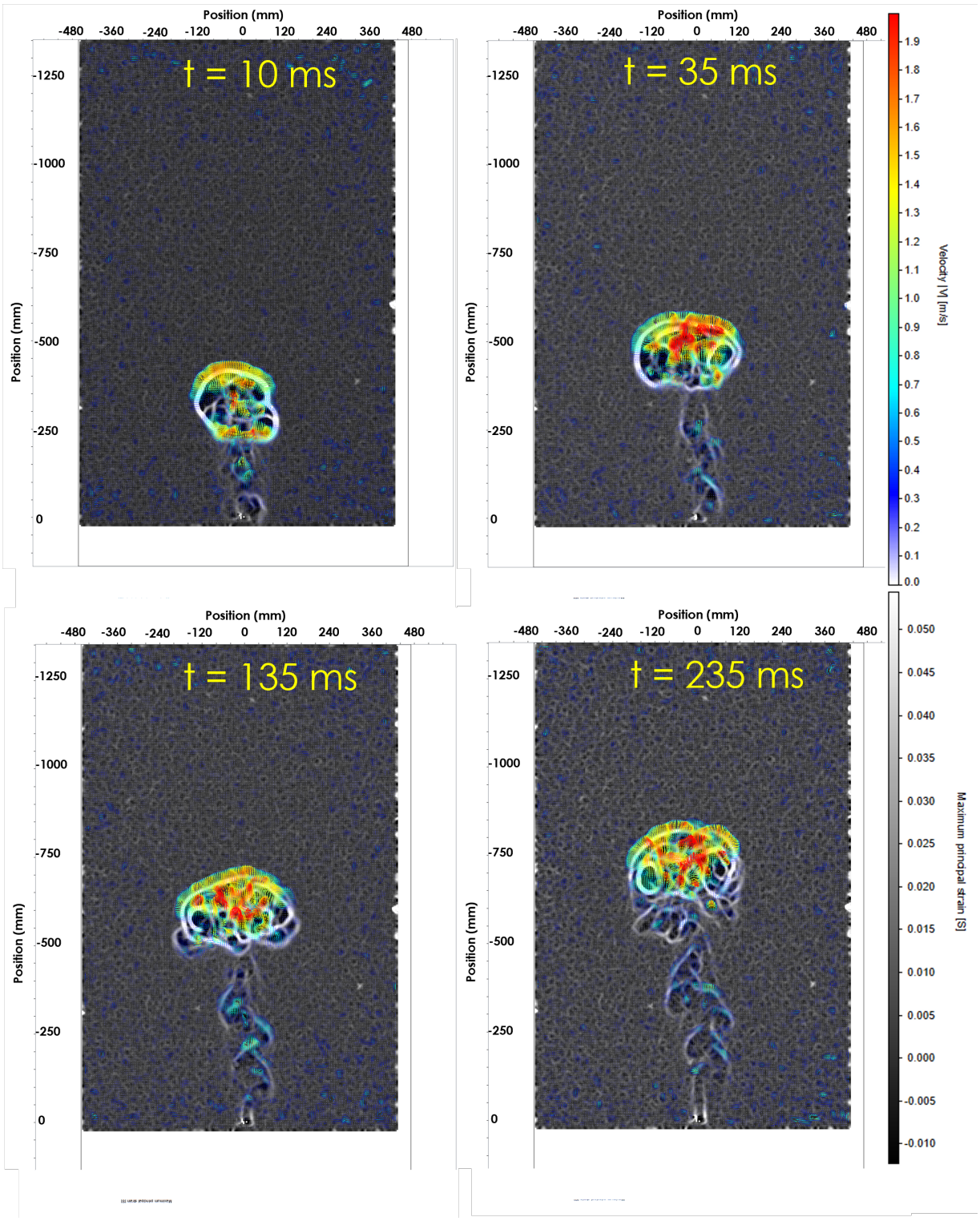

Figure 11. Experimental results from postprocessing BOS images. Gray scale contour displays maximum normal strain computed from the displacements shown in Figures 9–10, and the colored vectors illustrate the velocity magnitude of the extracted normal strain feature computed using PIV algorithms.

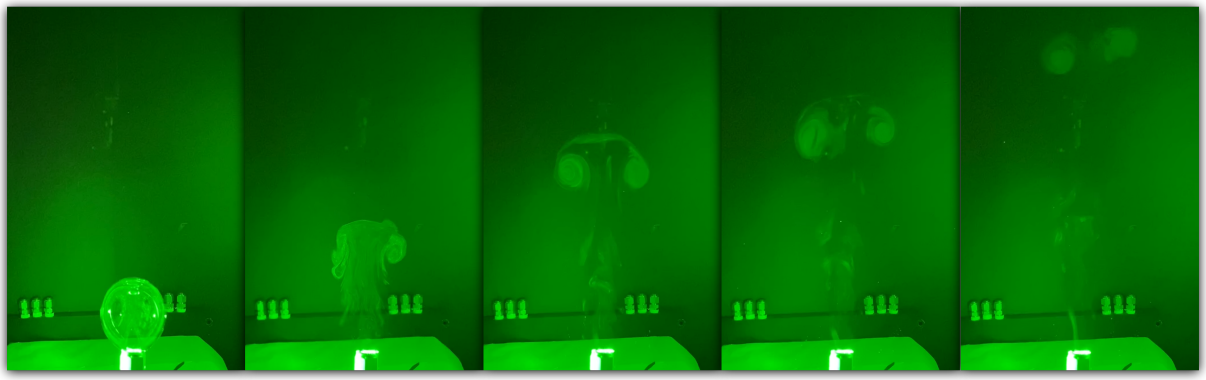

Figure 12. Image obtained from the attempted PIV visualization of helium bubbles filled with aerosol particles that are illuminated using a 15 Hz laser.

strain-rate images extracted from the BOS displacement results. Figure 11 illustrates the maximum normal strain using a gray scale scalar contour. This quantity was extracted from the displacement fields shown in Figures 9–10. An overlaid vector field depicts the velocity of the extracted features using PIV postprocessing algorithms. Results in Figure 11 show the vortex ring evolution is buoyancy-driven as the primary motion of the light gas cloud is in the opposite direction as gravity. The maximum velocity of the extracted features from the vortex ring was approximately 2 m/s.

A PIV feasibility study was also performed on the buoyant vortex ring flow. The results suggest that the following PIV approach would work well, and the effort identified instrumentation that would support acquisition of velocity fields at sufficiently high spatial and temporal resolutions.

For the PIV feasibility testing, the light gas bubble injection method was used. Before injecting the helium into the nozzle to grow the bubble, the gas was first seeded with particles by flowing it through an aerosol generator to entrain a liquid, diethylhexyl sebacate (DEHS), into particles. This configuration has been tested and generates aerosol particles with a mean diameter of 1 μm. After passing the light gas through the aerosol generator, the seeded gas was collected inside an accumulation chamber, which was situated between the aerosol generator and the bubble injection nozzle. A needle valve was used to control the mass flow from the accumulation chamber to the injection nozzle during the bubble growth process.

In general, an experimental setup for 2D two-component PIV measurements includes a laser, camera, synchronizer, and computer. The planar laser sheet illuminates the measured flow area, and the camera captures images of the scattered light from seeded particles within the flow. The recorded raw images are then postprocessed using PIV cross-correlation algorithms to identify particle displacements. This PIV feasibility study used a BigSky dual-head Nd:YAG laser, which is capable of double pulsing at 100 mJ, 15 Hz, and 532 nm. A combination of cylindrical and spherical lenses were aligned to collimate the beams and create a 1 mm thick laser sheet to illuminate the midplane of the helium-filled bubble. Figure 12 includes several images from the feasibility study of helium bubbles filled with DEHS 1 μm aerosol particles. The images shown in Figure 12 successfully illuminated the aerosol particles within the helium and revealed the cross section structures typical of a buoyant vortex ring. However, the 15 Hz maximum repetition rate of the available laser was insufficient to capture images with a small enough relative displacement such that PIV cross-correlation algorithms could be applied to generate velocity vector fields. The large time interval, Δt, between consecutive images would result in a poor estimation of the velocity.

This constraint indicates the necessity of a laser with high repetition rate to guarantee spatiotemporally resolved PIV measurements for a buoyant vortex ring.

4. NUMERICAL SIMULATIONS OF VORTEX RINGS

This section describes a numerical simulation effort to design the experimental facility's dimensions, investigate the feasibility of various light-to-heavy gas pairs, and gain a deeper understanding of the flow physics and evolution of the buoyant vortex ring 3D structures. Figure 13(a) presents the computational domain of the vortex ring study with a symmetrical boundary condition applied to reduce the computational cost. The domain had a horizontal cross section of 304.8×609.6 mm^2 (1×2 ft^2) and a height of 3,048 mm (10 ft). Figure 13(b) depicts the generated mesh. This size was determined to be acceptable for all gas pairs and can accommodate up to 100 mm diameter cups or bubbles without the introduction of wall effects on the buoyant flow.

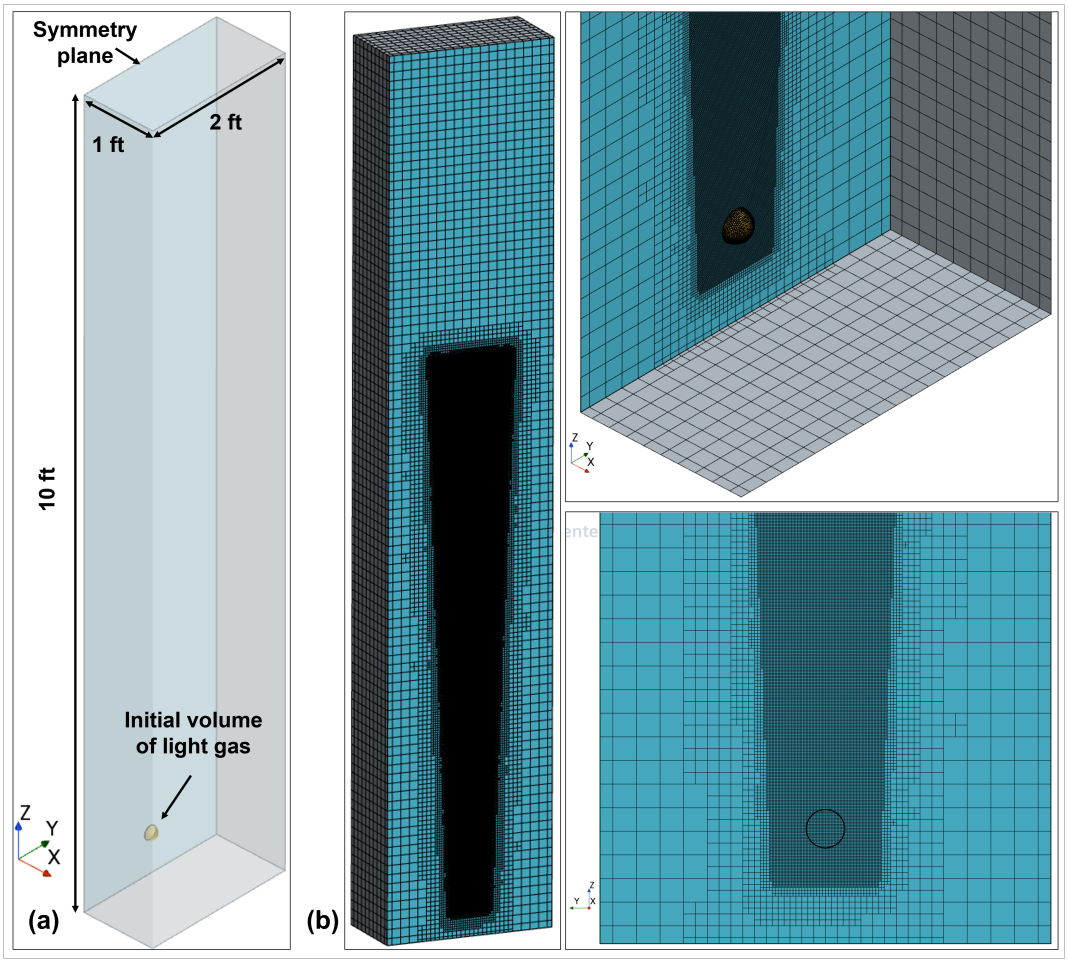

Figure 13. Numerical simulations of a vortex ring. (a) Computational domain. (b) Generated mesh.

Based on prior experience with various commercial and open source software, the commercial finite-volume CFD package STAR-CCM+ 2022.1.1 was selected for this study (Adapco (2022)). The software has an extensive user base, a set of validation studies, and is compliant with ASME NQA-1 for

nuclear industry customers.

The fluid-flow physics were modeled using a segregated flow with the implicit unsteady Reynolds-averaged Navier–Stokes $k - \omega$ shear-stress transport turbulence model (Menter (1994)) and low y^+ wall treatment. In the $k - \omega$ shear-stress transport model, a second-order convection scheme was applied. The volume of fluid (VOF) multiphase model (Hirt and Nichols (1981)) was chosen to simulate and identify the interface between light and heavy gases. The VOF model is suitable for model flows involving immiscible fluids, fluid mixtures, free surfaces, and phase contact on numerical grids capable of resolving the interface between the phases (Muzaferija (1998)). Because of its numerical efficiency, the VOF model is suited for simulations of flows in which each phase constitutes a large structure, with a relatively small total contact area between phases (Adapco (2022)).

In the VOF approach, the volume fraction is defined as the spatial distribution of each phase and is calculated by solving a transport equation for the phase volume fraction. To ensure numerical stability within the simulation, it is suggested that the Courant–Friedrichs–Lewy (CFL) number at the light-heavy gas interface should be limited to 1.

In this study, a second-order convection scheme was implemented along with high-resolution interface capturing options to accurately resolve the interfaces between the two gases. The second-order temporal discretization was selected, and a time step of 0.005 s was chosen over a simulation period. The interaction length scale model was applied with a primary and secondary regime interaction length scales of 1.587 and 0.158 mm, respectively. The Mixture Multiphase model was used to calculate the interaction between the light and heavy gases. This model can be used for an arbitrary combination of phases with any kind of phase interactions. Besides, if the mixture of phases can accurately represent the quantities of the individual phases, the Mixture Multiphase model can be used as an alternative to more numerically expensive Eulerian Multiphase simulations.

Mesh generation was performed using the automatic structured octree meshing capability in Star-CCM+. The Surface Remesher, Trimmed Cell Mesher, and Prism Layer Mesher were used. The Surface Remesher performed surface vertex retessellation of the 3D computational domain to optimize surface faces based on the target edge length and proximity refinements. The Trimmed Cell Mesher is best suited for use with the VOF model because of its ability to create anisotropic cells, which best discretize the interface between the two fluids. Moreover, the Trimmed Cell Mesher provides a robust and efficient method of producing a high-quality grid for both simple and complex mesh generation problems because it has highly desirable meshing attributes, including predominantly hexahedral mesh with minimal cell skew, the refinement based on surface mesh size and other user-defined refinement controls, surface quality independence, and alignment with a user-specified coordinate system. The Prism Layer Mesher generated a subsurface to extrude a set of prismatic cells from region surfaces into the core mesh. This layer of cells is necessary to improve the accuracy of the flow solution.

In Figure 14, CFD results of a buoyant vortex ring are illustrated. In this calculation, the light gas (helium) volume was initiated as a 50 mm diameter sphere in a heavy gas (nitrogen). Images of the vorticity isosurfaces at different time intervals reveal the formation of a vortex ring and its evolution.

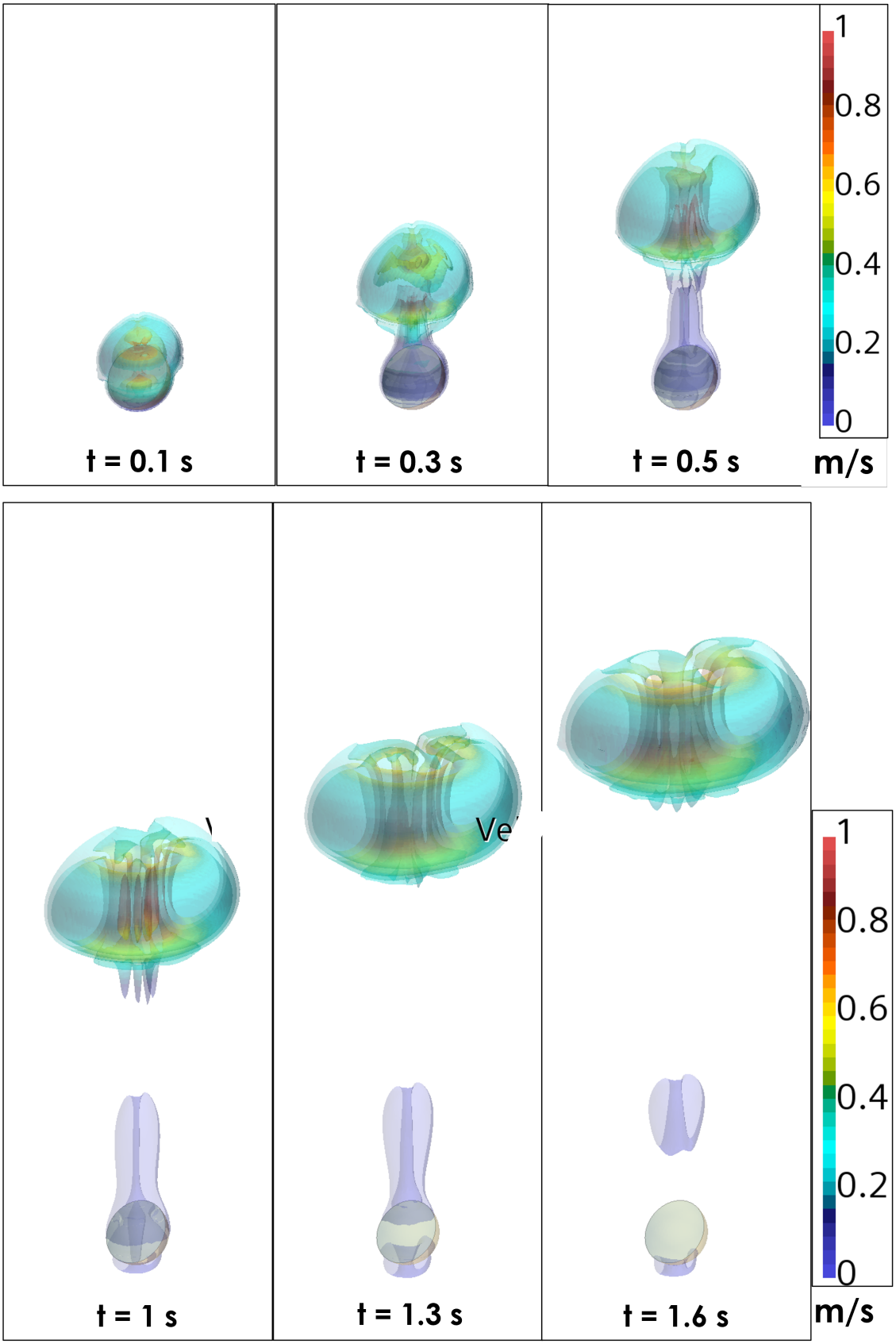

Figure 14. Buoyant vortex ring CFD solution of vorticity magnitude (Ω) isosurfaces Ω = 3 s^{-1}, 9 s^{-1}, and 21 s^{-1} from t = 0.1 to t = 1.6. The light gas (helium) volume was initialized as a 50 mm diameter sphere inside a heavy gas (nitrogen). Color contours show velocity magnitude (m/s).

5. CONCLUSIONS AND RECOMMENDATION FOR FUTURE WORK

This document summarizes the development of an experimental test facility to produce experimental measurements for the development and validation of numerical models of the nuclear cloud. The facility supports buoyant vortex rings with density ratios between the environment and the ring core ranging from 7 to 67 and encompassing relevant regimes for the problem of interest. In addition, 3D CFD simulations using the unsteady Reynolds-averaged Navier–Stokes VOF approach were performed to support the experimental design as well as provide insight about the formation and evolution of a vortex ring.

In summary, the vortex ring test facility has been successfully built and can be used to support flow visualization and measurements featuring nonintrusive techniques, such as BOS and PIV. In this effort, BOS has been successfully applied to buoyant vortex rings generated from the burst of helium-filled bubbles. The laser diagnostic technique of PIV has been proven to demonstrate the feasibility of obtaining the velocity field of the cloud and ring evolution using an aerosol generator to seed the light gas within the bubble.

To improve the spatial and temporal resolutions of the experimental PIV measurements, a high–repetition rate laser would allow for high-speed image acquisition and generation of spatiotemporally resolved velocity measurements suitable for this flow phenomena. Mixing phenomena between the light and heavy gases could be characterized using the laser-induced fluorescence technique, which may require the use of an ultraviolet laser. More complex volumetric measurements of velocity and density can be achieved using stereoscopic (2D three-component) and tomographic (3D three-component) PIV/BOS systems.

To add physical realism to the experimental procedure, several aspects can be considered:

1. A vertical density gradient of the heavy gas should be implemented, which would better represent the density gradient that exists in Earth's atmosphere. It would allow for the vortex ring to reach a stabilization elevation at which its density becomes equal to its local surroundings.
2. Lateral crossflow can be added to account for shear winds that are present in the atmosphere using slotted jets on the test section.
3. Effects of external turbulence to the cloud evolution processes can be experimentally investigated by passing the vortex ring over a thin plate or by using a towed grid to perturb the upstream condition above the cloud.
4. Entrainment and transport of dust and debris can be visualized and measured by seeding the near-ground volume with neutrally buoyant aerosol particles that will be pulled into the light gas as it rises. Lagrangian measurement techniques such as particle tracking velocimetry can be applied to quantify characteristics of dust and debris, such as mass, trajectory, and velocity.

To improve the resolution of the numerical simulations, the substitution of subgrid-scale resolved LES turbulence modeling instead of unsteady Reynolds-averaged Navier–Stokes would enable the resolution of finer-scale coherent structures within the cloud and vortex ring flow evolution. This may prove beneficial for capturing the entrainment rate phenomena and predicting the point of stabilization or neutral buoyancy with the atmosphere. The additional physical realism defined above for the experimental effort can also be added to any numerical effort.

6. ACKNOWLEDGMENTS

This work was funded by the Office of Nuclear Detonation Detection–Forensics Program within the US Department of Energy's National Nuclear Security Administration as part of the Rapid Response Research Venture.

7. REFERENCES

Adapco, C. (2022). STAR-CCM+ user's manual.

Arthur, R. S., Lundquist, K. A., Mirocha, J. D., Neuscamman, S., Kanarska, Y. and Nasstrom, J. S. (2021). Simulating nuclear cloud rise within a realistic atmosphere using the weather research and forecasting model, *Atmospheric Environment* **254**: 118363.

Bühlmann, P., Meier, A. H., Ehrensperger, M. and Rösgen, T. (2014). Laser speckle based background oriented schlieren measurements in a fire backlayering front, *The 17th International Symposium on Applications of Laser Techniques to Fluid Mechanic, Lisbon*, Vol. 29.

Caulfield, C. and Woods, A. W. (1998). Turbulent gravitational convection from a point source in a non-uniformly stratified environment, *Journal of Fluid Mechanics* **360**: 229–248.

Dorić, S. (1990). Ray tracing through gradient-index media: Recent improvements, *Applied optics* **29**(28): 4026–4029.

Foster, P. (1982). Particle fallout during plume rise, *Atmospheric Environment (1967)* **16**(12): 2777–2784.

Hirt, C. W. and Nichols, B. D. (1981). Volume of fluid (VOF) method for the dynamics of free boundaries, *Journal of Computational Physics* **39**(1): 201–225.

LaVision, G. (2022). Davis FlowMaster software manual for DaVis 10.2.

Menter, F. R. (1994). Two-equation eddy-viscosity turbulence models for engineering applications, *AIAA Journal* **32**(8): 1598–1605.

Moresco, P. (2022). A vorticity description of the nuclear cloud, *Technical Report ORNL/TM-2021/2110*.

Moresco, P., Harris, T. and Jodoin, V. (2014). Vorticity generation by the instantaneous release of energy near a reflective boundary, *Physical Review E* **90**(2): 023002.

Morton, B., Taylor, G. I. and Turner, J. S. (1956). Turbulent gravitational convection from maintained and instantaneous sources, *Proceedings of the Royal Society of London. Series A. Mathematical and Physical Sciences* **234**(1196): 1–23.

Muzaferija, S. (1998). Computation of free surface flows using interface-tracking and interface-capturing methods, *Nonlinear water-wave interaction. Computational Mechanics, Southampton.* pp. 1–42.

Raffel, M. (2015). Background-oriented schlieren (BOS) techniques, *Experiments in Fluids* **56**(3): 1–17.

Raffel, M., Willert, C. E. and Kompenhans, J. (1998). *Particle image velocimetry: A practical guide*, Vol. 2, Springer.

Scorer, R. S. (1957). Experiments on convection of isolated masses of buoyant fluid, *Journal of Fluid Mechanics* **2**(6): 583–594.

Settles, G. S. and Liberzon, A. (2022). Schlieren and BOS velocimetry of a round turbulent helium jet in air, *Optics and Lasers in Engineering* **156**: 107104.

Shariff, K. and Leonard, A. (1992). Vortex rings, *Annual Review of Fluid Mechanics* **24**(1): 235–279.

Sharma, A., Kumar, D. V. and Ghatak, A. K. (1982). Tracing rays through graded-index media: A new method, *Applied Optics* **21**(6): 984–987.

Thompson, R. S., Snyder, W. H. and Weil, J. C. (2000). Laboratory simulation of the rise of buoyant thermals created by open detonation, *Journal of Fluid Mechanics* **417**: 127–156.

Turner, J. S. (1957). Buoyant vortex rings, *Proceedings of the Royal Society of London. Series A. Mathematical and Physical Sciences* **239**(1216): 61–75.

Won, S. and Lee, C. (2020). Simulation of the mushroom cloud generated from a high-energy explosion using large-eddy simulation, *Journal of Mechanical Science and Technology* **34**(6): 2443–2453.

Xue, T., Rubinstein, M., Wadhwa, N., Levin, A., Durand, F. and Freeman, W. T. (2014). Refraction wiggles for measuring fluid depth and velocity from video, *European Conference on Computer Vision*, Springer, pp. 767–782.